ChemPubSoc Europe

DOI: 10.1002/celc.201800804

CHEMELECTROCHEM Articles

Low-Cost Aqueous Magnesium-Ion Battery Capacitor with Commercial Mn_3O_4 and Activated Carbon

Xi Cao,[a] Lulu Wang,[a] Jitao Chen,*[a] and Junrong Zheng*[a]

In this work, an aqueous rechargeable magnesium-ion battery capacitor with low cost and great application potential is constructed for the first time by using commercial spinel Mn_3O_4 as the cathode, coupling with activated carbon as the anode. Spinel Mn_3O_4 experiences a phase transformation to layered Birnessite nanoflakes during the electrochemical process in aqueous $MgSO_4$ electrolyte, which acts as the actual cathode material. By decreasing the particle size of commercial Mn_3O_4 from several micrometers to about 50–100 nm through a facile milling method, the nanoparticles can more easily experience the phase transformation, which results in significantly enhanced electrochemical properties, with a high reversible capacity of about 81 $mAh{\cdot}g^{-1}$ at a current density of 0.5 $A\,g^{-1}$ after 300 cycles in a three-electrode system. For comparison, the Mn_3O_4 without milling exhibits only 33 $mAh\,g^{-1}$. Coupling with activated carbon, the full cell also exhibits excellent rate and cycle performance; for example, even after 6000 cycles at the rate of 0.5 $A\,g^{-1}$, it still delivers a high capacity of about 81 $mAh\,g^{-1}$. Such outstanding electrochemical properties are obtained without adding high cost components such as graphene or forming complex nanostructures. Its low cost and scalable preparation procedure make this approach very promising for safe energy storage.

1. Introduction

In order to take full advantages of renewable power sources such as natural wind and solar, many researchers have focused on the study of energy storage technologies and their practical applications, among them, rechargeable batteries with high power, long cycle life and high energy efficiency become an important field for electric energy storage.[1–5] Benefit from the extensive and in-depth research, lithium-ion batteries have shown significant improvement in energy density and cycle life. However, the explosion risk and the high price still need to be solved.[6,7]

To overcome the safety issues, aqueous rechargeable batteries have been invented in recent years with advantages of special safety, low cost and high rate capability.[8–22] Porous $LiMn_2O_4$ prepared by template method exhibits an excellent cycling performance with the capacity retention of 93% after 10000 cycles at 9 C.[11] $LiMn_2O_4$ nanotube with a preferred orientation of (400) planes prepared by using multiwall carbon nanotubes as a sacrificial template also displays superfast charge/discharge capability (600 C, 53.9% capacity) with excellent cycling performance.[12] By using coated lithium metal as the stable anode in aqueous electrolytes, combining with $LiMn_2O_4$ as the cathode, this ARLB delivers an output voltage of about 4.0 V, which is a big breakthrough of the theoretic stable window of water (1.23 V).[13] Aqueous rechargeable sodium batteries (ARSBs) have also gained attentions due to the abundant sodium reserves.[14–22] However, the radius of sodium ion is much larger than that of the lithium ion, which makes it more difficult to find appropriate cathode to accommodate Na^+. For example, Na–Mn–O oxides with different crystal structures and morphologies have been developed, however, most of them suffers from poor storage capability, low voltage plateau or poor cyclability.[15,19,20] Other novel system, such as rechargeable magnesium batteries using Mg in Grignard reagent-based electrolyte as the negative electrode, a lithium intercalation compound in aqueous solution as the positive electrode,[23] aqueous rechargeable zinc//aluminum ion battery,[24] quasi-solid-state sodium-ion capacitor,[25] $LiMn_2O_4$//Ti_3C_2Tx lithium ion capacitor battery and MnO_2//Ti_3C_2Tx sodium ion capacitor battery[26] also display capable capacities, remarkable rate capabilities, and excellent cycling performances.

As another promising system, aqueous rechargeable magnesium batteries (ARMBs) system is also explored due to its similar electrochemical characteristics to lithium and low cost. However, only a handful of reports concerning ARMBs are available.[27–30] For example, nanowire Mg-OMS-2/Graphene composite was prepared by hydrothermal method and used as the cathode material in an aqueous magnesium ion battery capacitor which included activated carbon as the anode.[27] Also, as the traditional anode for lithium ion batteries,[31,32] it was recently reported that spinel Mn_3O_4 may experience a phase transition to crystal-water-containing layered Birnessite MnO_2 during an electrochemical process in aqueous $MgSO_4$ electrolyte with a high capacity.[27,28,33,34] However, until now, none of the reported aqueous rechargeable magnesium battery systems has obvious commercial potential mainly due to the costly material preparation methods.

In this work, commercial spinel Mn_3O_4 is studied as the magnesium storage materials in aqueous solutions. In the three electrode system, Mn_3O_4 after milling demonstrates an excellent

[a] Dr. X. Cao, Dr. L. Wang, Prof. J. Chen, Prof. J. Zheng
College of Chemistry and Molecular Engineering
Peking University, Beijing 100871 China
E-mail: junrong@pku.edu.cn
chenjitao@pku.edu.cn

Supporting information for this article is available on the WWW under https://doi.org/10.1002/celc.201800804

rate and cycle performance, which gives a high reversible capacity of about 81 mAh g^{-1} at the current density of 0.5 A g^{-1} after 300 cycles. More importantly, scalable Mn_3O_4//Activated Carbon aqueous rechargeable magnesium ion battery capacitor system is first assembled in this work. In the full cell, Mn_3O_4 after milling demonstrates a high reversible capacity to be about 82 mAh g^{-1} even after a super-long 6000 cycles at the high rate of 0.5 A g^{-1}.

Experimental Section

Materials Preparation and Characterization

The commercial Mn_3O_4 (denoted as Mn_3O_4–C) is bought from WoKai Chem. Placing commercial Mn_3O_4 into a horizontal ball mill (with the diameter of milling media to be about 0.5 mm) and milled for 2 hours at the speed of 2500 r/min in ethanol solution, Mn_3O_4 nanoparticles are obtained (denoted as Mn_3O_4–M). Activated carbon is bought from YiHuan Carbon (YEC-8A) and used without further purification.

X-ray diffractometer (XRD, Rigaku) with Cu Ka radiation (λ = 0.151 417 8 nm) is used to determine the crystal structure of the active materials. Transmission electron microscopy (TEM) measurements are conducted on a H9000NAR microscope (Hitachi, Japan) equipped with a cold field-emission gun operating at 200 kV accelerating voltage. The scanning electron microscopy (SEM) is performed to investigate the morphology of the electrode before and after electrochemical cycling. X-ray photoelectron spectroscopy (XPS) analysis is performed using a Surface Science Instruments S-probe spectrometer with a monochromatized Al Ka X-ray and a low-energy electron flood gun for charge neutralization. The accelerating voltage and current are 40 kV and 40 mA, respectively.

Electrochemical Measurement of the Cathode

The prepared cathode slurry consists of 10% acetylene black, 10% polyvinylidene difluoride (PVDF) binder and 80% Mn_3O_4–C/ Mn_3O_4–M dispersed in 1-methyl-2-pyrrolidone (NMP). The obtained electrodes are prepared by coating the slurry onto graphite paper with a mass loadings of active material about 5 mg cm^{-2}, then drying in vacuum at 80 °C for 24 h. LAND Battery Testing system (model CT2001A, Land, China) are used for the galvanostatic charge and discharge tests. The electrochemical workstation (CHI 650C, USA) is used to test cyclic voltammetry (CV) and impedance. The electrochemical tests of Mn_3O_4–C and Mn_3O_4–M are performed by utilizing a conventional standard three-electrode system including a working electrode, a counter electrode (Pt sheet) and a reference electrode (Ag/AgCl) in 2 mol L^{-1} $MgSO_4$ electrolyte.

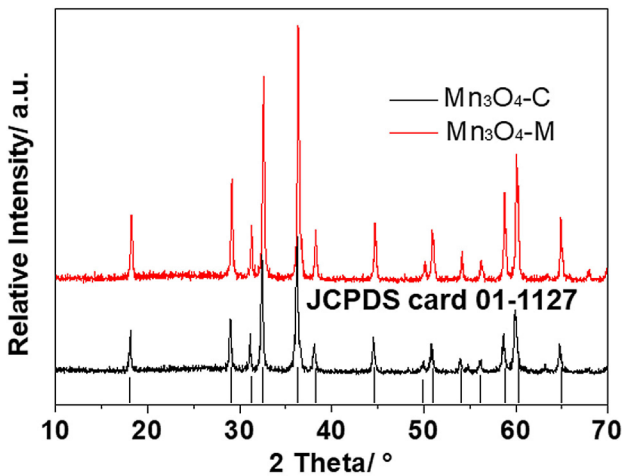

Figure 1. a) X-ray diffraction patterns of Mn_3O_4–C and Mn_3O_4–M.

Electrochemical Measurement of Spinel Mn_3O_4//Activated Carbon Full Cell

The anode electrode is prepared in the same way with the Mn_3O_4 cathode side except the mass loading of active material is about 10 mg cm^{-2}. The full cell is fabricated by cathode, anode and a filter paper as the traditional battery separator in sandwich-type coin cells. The two electrodes are immersed in 2 mol L^{-1} $MgSO_4$ electrolyte, which is bubbled by nitrogen for 1 h to exclude oxygen before measures. In order to investigate the actual application potential of this system, pouch cell is also assembled and tested, with the mass loadings of the cathode material about 15 mg cm^{-2}.

2. Results and Discussion

2.1. Characterization of the Spinel Mn_3O_4

The X-ray diffraction patterns of Mn_3O_4–C and Mn_3O_4–M are shown in Figure 1. The two samples, of which crystal structure could be assigned to the tetragonal space group I41/amd, maintain the crystal type of spinel Mn_3O_4 without any purities and match very well with the standard crystallographic tables (JCPDS card 01-1127).[35,36]

The detailed morphology of Mn_3O_4–C and Mn_3O_4–M are characterized by scanning electron microscopy (SEM), as shown in Figure 2. As we can see, the commercial Mn_3O_4 before milling

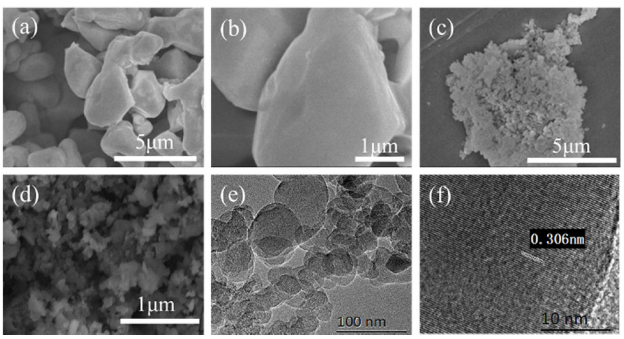

Figure 2. a, b) SEM image of Mn_3O_4–C; c, d) Mn_3O_4–M; e) TEM and f) HRTEM image of Mn_3O_4–M.

exhibits a broad size distribution of about several micrometers, however, after milling in ethanol media, the particle size reduces to about 50-100 nm.

The TEM image of Mn_3O_4 after milling is shown in Figure 2e, the morphology and particle size are consistent with the SEM results. Figure 2f shows the HRTEM image, it can be observed that the d spacing of lattice fringes is 0.306 nm, corresponding to the (101) plane from the peak at $2\theta = 28.7^\circ$ in XRD pattern.

2.2. Electrochemical Performance

In 2 mol L^{-1} $MgSO_4$ electrolyte, Mn_3O_4-M nanoparticles gradually transform into lamellar structures consisting of nanosheets after 30 cycles at a current density of 0.1 A g^{-1} in the potential range from −0.2 to + 1.0 V,[35,37,38] as shown in Figure 3a &b. However,

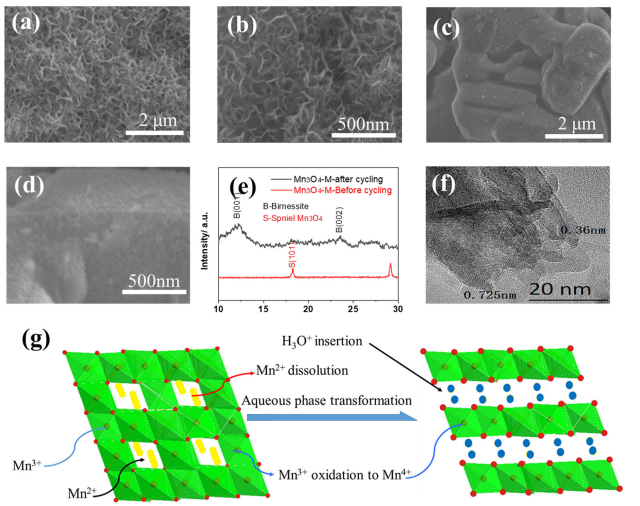

Figure 3. SEM morphology of Mn_3O_4–M (a, b) and Mn_3O_4–C (c, d) electrode after 30 charge/discharge cycles in three-electrode system; XRD patterns of Mn_3O_4–M before and after 30 cycles (e); TEM image of Mn_3O_4–M after cycling (f); The phase transformation of Mn_3O_4 to crystal-water-containing layered Birnessite MnO_2 in aqueous $MgSO_4$ electrolyte solutions (g).

the non-milled cathode largely maintains intact (Figure 3c) except partially forming nanosheets on the surface of the big particles (Figure 3d), which suggests that only the part close to the surface participate in the phase/structure changes. The similar results have also been reported before, Choi[33] revealed that the phase transition was mediated by formation of a transition phase at the phase boundary. The phase transition progresses with layer-by-layer propagation of the transient phase toward the original spinel. Once the spinel-to-Birnessite phase transition progresses over about 10 nm, the already grown Birnessite layers tend to peel off. In this way, due to their small portions of surface, the phase transition of large spinel particles would be inefficient, especially at high rates. Thus, most of the large spinel particles would be activated very slow, and largely maintain intact. By decreasing the particle size, the phase transformation would be facilitated, and the activation process would be completed in the first several cycles, showing an enhanced electrochemical performance. What is more, by decreasing the particle size, the contact area between the active materials and the conductive carbon can be increased, the whole electro conductivity of the electrode can also be improved, with the decreased impedance.

These nanosheets are further investigated with XRD and TEM. As we can see from Figure 3e, after cycling, the diffraction peak refers to (101) peak of spinel-Mn_3O_4 at 18.3° disappears, while the peaks corresponding to layered-Birnessite MnO_2 appear, confirming the phase transformation from spinel-Mn_3O_4 to crystal-water-containing layered Birnessite MnO_2. The (001) peak at 12.3° indicates that the layer-to-layer distance between octahedral MnO_6 is 7.25 Å, reflecting the presence of crystal water between the MnO_6 layers. The d spacing of lattice fringes of layered-Birnessite 0.725 and 0.36 nm can be clearly observed from HRTEM image (Figure 3f).

Figure 3g illustrates the phase transition process, at the initial stage, crystal water is inserted into the interlayer space between MnO_6 layers, accompanied with Mn^{2+} dissolute into the solution and the oxidation of Mn^{3+} to Mn^{4+}.[27,33] This result can be confirmed by the EDS results, after the first charge in $MgSO_4$ electrolyte, as shown in Figure S1a, almost no Mg can be found in the electrode, indicating that the inserted Mg content is negligible. However, Mg^{2+} would prefer to insert into the cathode to form the Mg-Birnessite in the discharge process, as evidenced in Figure S1b, with the increase of Mg content in the electrode material.

These reactions can be summarized as follows:

$$Mn_3O_4 + xH_2O \rightarrow Mn^{2+} + \text{Birnessite-}MnO_2 \cdot xH_2O$$

$$\text{Birnessite-}MnO_2 \cdot xH_2O + Mg^{2+} + yH_2O \leftrightarrow \text{Mg-Birnessite-}MnO_2 \cdot (x+y)H_2O$$

Except the EDS tests, we also conduct the XRD and XPS characterization to reveal the insertion/extraction mechanism of Mg^{2+}. The XRD patterns of the cathode after charge and discharge in 2 M $MgSO_4$ are shown in Figure S2a, the pattern after charge displays the XRD peaks corresponding to Birnessite MnO_2 with obvious (001) and (002) peaks. The (001) peak disappears after the discharge, but the (002) peak is still preserved, suggesting that a new lattice arrangement after cations insertion still maintains the (002) plane regularity. The similar results have been reported by Choi before,[27] in their work, ABF-STEM was carried out in order to visualize the structure of discharged cathodes at the atomic level, the results showed that the interlayer spacing of the discharged phase was half of the (001) spacing, consistent with the preserved (002) peak in the XRD analysis, moreover, the ABF-STEM image showed that Mn and Mg do not exist in separate layers but rather in a mixed state in each layer. By comparing the XPS spectra of the cathode after charge and discharge, as shown in Figure S2b, we can obtain the same results with the EDS results, that is, after the charge process, Mg would not insert into the cathode; while after the discharge, Mg is inserted into the cathode.

The electrochemical behavior of Mg^{2+} insertion/deinsertion in Mn_3O_4–C and Mn_3O_4–M is investigated by cyclic voltammetry (CV) at different scan rates in a wider potential range from −0.4 to + 1.0 V in three-electrode system. It is obvious that two oxidation peaks at around 0.5 V and 0.3 V appear in Figure 4, corresponding to the process of Mg^{2+} deinsertion from the cathode, while the wide reduction peak at around 0 V corresponds to the Mg^{2+} insertion into the cathode. The higher current densities of Mn_3O_4–M (Figure 4a) than that of Mn_3O_4–C (Figure 4b), further confirms that decreasing the particle size facilitates the reactions.

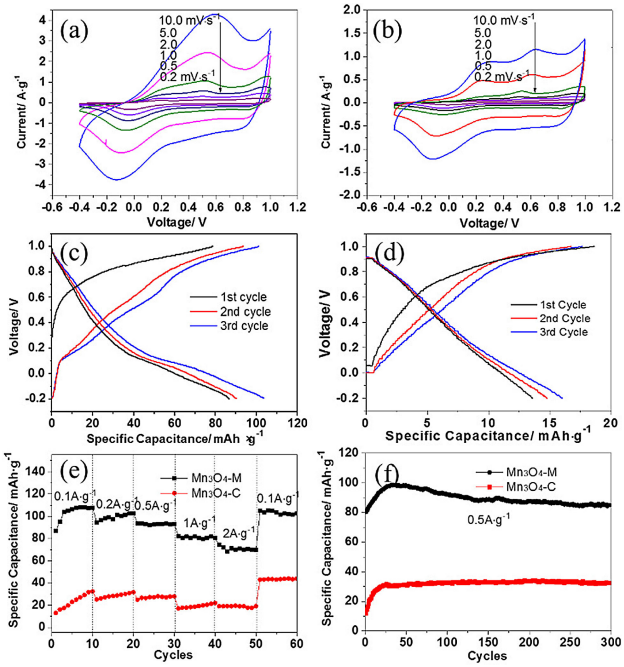

Figure 4. Cyclic voltammetry (CV) of a) Mn_3O_4–M and b) Mn_3O_4–C at different scan rates; charge and discharge of c) Mn_3O_4–M and d) Mn_3O_4–C at the current density of 0.1 A g^{-1}; e) rate and f) cycle performance of Mn_3O_4–M and Mn_3O_4–C in three-electrode system.

The rate performance at various charge-discharge rates are also evaluated and compared. As shown in Figure 4c, Mn_3O_4–M is found to demonstrate higher reversible capacities compared to Mn_3O_4–C at each current density. It presents a higher reversible capacity of approximately 105.8 mAh g^{-1} at a current density of 0.1 A g^{-1}. With increasing current density, the specific discharge capacities decrease to be 93.2, 79.8 and 68.5 mAh g^{-1} at rates of 0.5 A g^{-1}, 1 A g^{-1} and 2 A g^{-1} respectively. When the current density decreases to 0.1 A g^{-1}, the capacity goes up to about 103 mAh g^{-1}, indicating a good rate capability and electrode structure stability. However, Mn_3O_4–C delivers only 41 mAh g^{-1} at the current density of 0.1 A g^{-1}. The cycle performance of both Mn_3O_4–C and Mn_3O_4–M are evaluated for 300 cycles at the high current density of 0.5 A g^{-1}, as shown in Figure 4d. Clearly, the Mn_3O_4–M electrodes show better cycle performance than Mn_3O_4–C, with the reversible specific capacitance slightly increases to almost 100 mAh g^{-1} and can maintain about 81 mAh g^{-1} after 300 cycles, which is more than twice of Mn_3O_4–C. Compared with other materials synthesized through complex strategies, both rate and cycling performance of the spinel Mn_3O_4 prepared by this simply wet milling method is very remarkable (listed in Table S1).

The XPS analyses are carried out to investigate the oxidation state of Mn in Mn_3O_4 and charged/discharged Birnessite MnO_2, as shown in Figure 5. In the case of Mn_3O_4–M, the Mn 2p3/2 peak centered at 641.48 eV and the Mn 2p1/2 peak at 653.3 eV, with the spin-orbit splitting is 11.82 eV, the feature peaks of Mn_3O_4,[38–40] further confirm that the particles before cycling are Mn_3O_4. Further, after charge, the detected peak at the binding energy of 642.4 eV corresponding to Mn

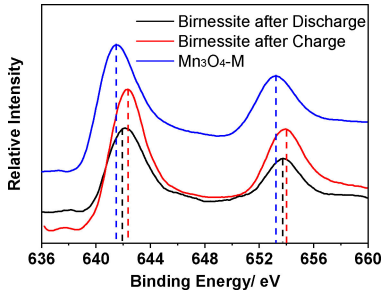

Figure 5. The XPS result of Mn_3O_4–M and Birnessite after charge and discharge.

2p3/2 indicates that the element Mn is present in the chemical state of Mn^{4+}.[40,42] The peak appears at the binding energy of 654 eV assigned to Mn 2p1/2 suggests the sole existence of Mn^{4+}.[41] After discharge, the two main peaks shift to the binding energy of 653.6 and 641.8 eV, which is associated with the coexistence of Mn^{3+} and Mn^{4+} species, in accordance with the results reported in the literatures,[28,30,41,42] which suggests the insertion of Mg^{2+} ions by the changed valence of manganese during the discharge process.

2.3. Electrochemical Performance of the Mn_3O_4//AC Full Cell

The aqueous rechargeable magnesium battery capacitor system using spinel Mn_3O_4 as the cathode material, activated carbon as the anode material and 2 mol L^{-1} $MgSO_4$ as the electrolyte is assembled. The CV curves of the activated carbon (AC) within the potential range from −1.0 to −0.2 V (vs. Ag/AgCl) in a three-electrode system are shown in Figure S3a, which exhibited the typical rectangular shape of the electrochemical double layer capacitor. The discharge process corresponds to the electrostatic adsorption of Mg^{2+} on the surface of the AC, while the charge process corresponds to the desorption of Mg^{2+} on the surface of the AC. The CV curves at different scan rates remain the same shape, also suggesting an excellent rate performance. The rate performance of AC electrode is also shown in Figure S3b & c, remarkably, the reversible capacity of AC almost remains at ca. 50 mAh g^{-1} even at different current densities. Based on the specific capacitance of both sides, the weight ratio of Mn_3O_4 to AC is set as ~1:2. The potential-time curves of Mn_3O_4–M and AC electrodes vs Ag/AgCl reference electrode, and the charge/discharge-time curves of the full cell at the current density of 0.1 A g^{-1} are shown in Figure 6a. The cathode presents obviously different charge/discharge curves from the AC anode, which exhibits typical battery characteristics with plateaus, representing Mg^{2+} inserting/deinserting into/from the cathode in the voltage range of −0.2 – +1.0 V. While the AC anode presents the typical capacitor characteristic. By assembling these two materials together in a full cell, the voltage range can be as high as 2V.

Figure 6b exhibits the CV curves of Mn_3O_4–M//AC full cell in 2 mol L^{-1} $MgSO_4$ electrolytes at scan rates of 0.2, 0.5, 1, 2 mV s^{-1} in the potential range from 0 to +2.0 V. It is obvious that the

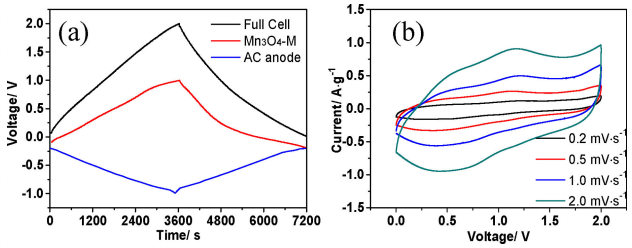

Figure 6. a) Potential-time curves of the cathode and anode vs Ag/AgCl; b) CV curves of Mn_3O_4–M//AC full cell at scan rates of 0.2, 0.5, 1.0, 2.0 mV s^{-1}.

broad oxidation peak in the range of 0.5 V to 1.1 V corresponds to the extraction process of Mg^{2+} from the cathode and the adsorption of Mg^{2+} in the AC, while the wide reduction peak below 1.0 V corresponds to the insertion process of Mg^{2+} into cathode and the desorption of Mg^{2+} from AC, which is similar to the $LiMn_2O_4$//AC system,[43] as illustrated in Scheme 1. The CV

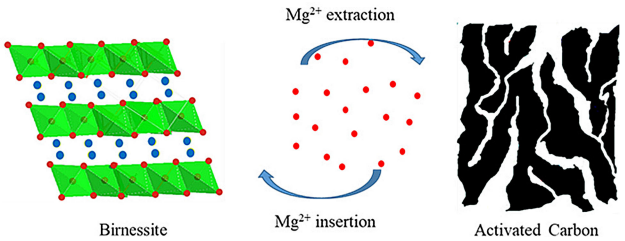

Scheme 1. Schematics of Mn_3O_4//AC full cell using Mn_3O_4 as the cathode and AC as the anode.

curves remain similar at different scan rates, indicating a good reversibility.

Similar to the three-electrode result, the full cell delivers a capacity of approximately 102.5 mAh g^{-1} at a current density of 0.1 A g^{-1} based on the mass of cathode. With increasing current density, the specific discharge capacities are 86, 80 and 69 mAh g^{-1} at rates of 0.5 A g^{-1}, 1 A g^{-1} and 2 A g^{-1}, respectively (Figure 7a). The cycle performance is evaluated for 200 cycles at

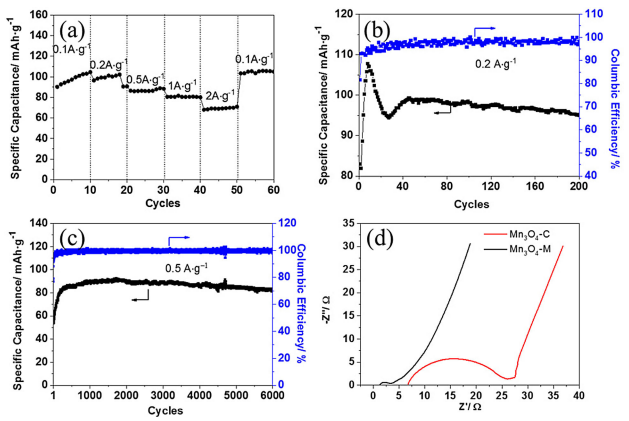

Figure 7. a) Rate and b, c) cycle performance of Mn_3O_4–M//AC full cell; d) Nyquist plots of the Mn_3O_4–C//AC and Mn_3O_4–M//AC full cell after 30 cycles.

the current density of 0.2 A g^{-1}, as shown in Figure 7b, the Mn_3O_4–M//AC shows a high reversible capacity about 95 mAh g^{-1} after 200 cycles. Moreover, Mn_3O_4–M//AC full cell also exhibits excellent long-term cycling stability, as displayed in Figure 7c, even after 6000 cycles at a high rate of 0.5 A g^{-1}, it still retains the capacity of 82 mAh g^{-1} with nearly 100% coulombic efficiency. Taking into account the total mass of both cathode and anode active materials, the specific energy of the cells can reach 20.2 Wh kg^{-1} at a power density of 125 W kg^{-1}, which is a much larger than the carbon based capacitors.

Nyquist plots of Mn_3O_4–C and Mn_3O_4–M electrodes after 30 charge/discharge cycles at 0.1 A g^{-1} are shown in Figure 7d. Typically, the semicircle in the high frequency region is associated with the surface film (R_f) and the charge transfer resistance (R_{ct}).[44] As we can see, it is obvious that the radii of the semicircle ($R_f + R_{ct}$) of Mn_3O_4–M is much smaller than that of the Mn_3O_4–C, which indicates that Mn_3O_4–M is more capable of tolerating the fast charge and discharge reactions.

In order to investigate the actual application potential of this system, a pouch cell is also assembled and tested, with the mass loadings of the cathode material about 15 mg cm^{-2}, as shown in Figure 8 (inset). Even at high rates (0.5 A g^{-1}), it still

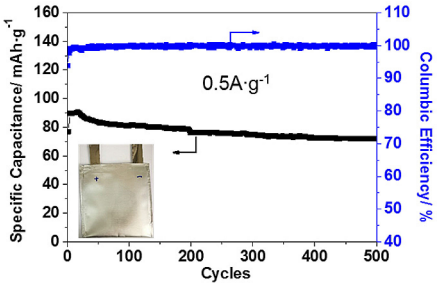

Figure 8. Cycle performance of Mn_3O_4–M//AC pouch cell at 0.5 A g^{-1} (inset: the pouch cell).

retains the capacity of 70 mAh g^{-1} after 500 cycles with nearly 100% coulombic efficiency and 80% of the initial capacity, exhibiting an excellent cycling stability. Such outstanding electrochemical properties are obtained without adding any high cost components such as graphene or nanotubes or forming complex nanostructures.

3. Conclusions

In summary, spinel Mn_3O_4 with particle size about 50–100 nm is obtained by wet milling commercial Mn_3O_4. Both of Mn_3O_4 before and after milling are studied as the magnesium storage materials in aqueous solutions. By decreasing the particle size into nanoscale, the electrochemical properties are greatly enhanced, e.g., the milled Mn_3O_4 shows a much better rate and cycle performance with a high reversible capacity of approximately 105.8 mAh g^{-1} at a current density of 0.1 A g^{-1}in three-electrode system. Even at a high rate of 1 A g^{-1}, the Mn_3O_4-M shows a high capacity of 79.8 mAh g^{-1}, which is twice of the

Mn_3O_4–C. Moreover, for the first time, the aqueous rechargeable magnesium ions battery capacitor with excellent electrochemical performance is successfully assembled by using Mn_3O_4–M as the cathode and activated carbon as the anode, with a high energy density of 20.2 Wh Kg^{-1} even after 6000 cycles at a power density of 125 W kg^{-1}. The low cost and ease of preparation make this approach very promising for applications in the energy storage systems.

Acknowledgements

This work is supported by the National Natural Science Foundation of China (NSFC-21673004, 21673008), MOST (2017YFA0204702) China, the National Key Research and Development Program of China (2016YFB0700604) and China Postdoctoral Science Foundation (2017M610017).

Conflict of Interest

The authors declare no conflict of interest.

Keywords: Mn_3O_4 · activated carbon · magnesium ions · aqueous battery capacitors · high capacity

[1] M. Armand, J. M. Tarascon, *Nature* **2008**, *451*, 652–657.
[2] B. Dunn, H. Kamath, J. M. Tarascon, *Science* **2011**, *334*, 928–935.
[3] S. R. Gowda, V. Pushparaj, S. Herle, G. Girishkumar, J. G. Gordon, H. Gullapalli, X. Zhan, P. M. Ajayan, A. L. M. Reddy, *Nano Lett.* **2012**, *12*, 6060–6065.
[4] P. Simon, Y. Gogotsi, *Nat. Mater.* **2008**, *7*, 845–854.
[5] J. R. Szczech, S. Jin, *Energy Environ. Sci.* **2011**, *4*, 56–72
[6] S. Chu, A. Majumdar, *Nature* **2012**, *488*, 294–303.
[7] J. B. Goodenough, K. S. Park, *J. Am. Chem. Soc.* **2013**, *135*, 1167–1176.
[8] Z. Chang, Y. Q. Yang, M. X. Li, X. W. Wang, Y. P. Wu, *J. Mater. Chem. A* **2014**, *2*, 10739–10755.
[9] H. L. Wang, Y. Y. Liang, M. Gong, Y. G. Li, W. Chang, T. Mefford, J. Zhou, J. Wang, T. Regier, F. Wei, H. J. Dai, *Nat. Commun.* **2012**, *3*, 917.
[10] M. Gong, Y. G. Li, H. B. Zhang, B. Zhang, W. Zhou, J. Feng, H. L. Wang, Y. Y. Liang, Z. J. Fan, J. Liu, H. J. Dai, *Energy Environ. Sci.* **2014**, *7*, 2025–2032.
[11] Q. T. Qu, L. J. Fu, X. Y. Zhan, D. Samuelis, J. Maier, L. Li, S. Tian, Z. H. Li, Y. P. Wu, *Energy Environ. Sci.* **2011**, *4*, 3985–3990.
[12] W. Tang, Y. Y. Hou, F. X. Wang, L. L. Liu, Y. P. Wu, K. Zhu, *Nano Lett.* **2013**, *13*, 2036–2040.
[13] X. J. Wang, Y. Y. Hou, Y. S. Zhu, Y. P. Wu, R. Holze, *Sci. Rep.* **2013**, *3*, 1401.
[14] Z. Li, D. Young, K. Xiang, W. C. Carter, Y. M. Chiang, *Adv. Energy Mater.* **2013**, *3*, 290–294.
[15] J. F. Whitacre, A. Tevar, S. Sharma, *Electrochem. Commun.* **2010**, *12*, 463–466.
[16] V. Palomares, P. Serras, I. Villaluenga, K. B. Hueso, J. Carretero-Gonzalez, T. Rojo, *Energy Environ. Sci.* **2012**, *5*, 5884–5901.
[17] H. L. Pan, Y. S. Hu, L. Q. Chen, *Energy Environ. Sci.* **2013**, *6*, 2338–2360.
[18] Y. Liu, Y. Qiao, W. X. Zhang, H. H. Xu, Z. Li, Y. Shen, L. X. Yuan, X. L. Hu, X. Dai, Y. H. Huang, *Nano Energy* **2014**, *5*, 97–104.
[19] Y. S. Wang, J. Liu, B. J. Lee, R. M. Qiao, Z. Z. Yang, S. Y. Xu, X. Q. Yu, L. Gu, Y. S. Hu, W. L. Yang, K. Kang, H. Li, X. Q. Yang, L. Q. Chen, X. J. Huang, *Nat. Commun.* **2015**, *6*, 6401.
[20] Y. S. Wang, L. Q. Mu, J. Liu, Z. Z. Yang, X. Q. Yu, L. Gu, Y. S. Hu, H. Li, X. Q. Yang, L. Q. Chen, X. J. Huang, *Adv. Energy Mater.* **2015**, *5*, 1501005.
[21] X. L. Dong, L. Chen, J. Y. Liu, S. Haller, Y. G. Wang, Y. Y. Xia, *Sci. Adv.* **2016**, *2*, 1501038.
[22] X. Q. Zhang, Z. G. Hou, X. N. Li, J. W. Liang, Y. C. Zhu, Y. T. Qian, *J. Mater. Chem. A* **2016**, *4*, 856–860.
[23] Z. Chang, Y. Q. Yang, X. W. Wang, M. X. Li, Z. W. Fu, Y. P. Wu, R. Holze, *Sci. Rep.* **2015**, *5*, 11931.
[24] F. X. Wang, F. Yu, X. W. Wang, Z. Chang, L. J. Fu, Y. S. Zhu, Z. B. Wen, Y. P. Wu, W. Huang, *ACS Appl. Mater. Interfaces* **2016**, *8*, 9022–9029.
[25] F. X. Wang, X. W. Wang, Z. Chang, X. W. Wu, X. Liu, L. J. Fu, Y. S. Zhu, Y. P. Wu, W. Huang, *Adv. Mater.* **2015**, *27*, 6962–6968.
[26] K. Zhu, H. Y. Zhang, K. Ye, W. B. Zhao, J. Yan, K. Cheng, G. L. Wang, B. F. Yang, D. X. Cao, *ChemElectroChem.* **2017**, *4*, 3018–3025.
[27] K. W. Nam, S. Kim, S. Lee, M. Salama, I. Shterenberg, Y. Gofer, J. S. Kim, E. Yang, C. S. Park, J. S. Kim, S. S. Lee, W. S. Chang, S. G. Doo, Y. N. Jo, Y. Jung, D. Aurbach, J. W. Choi, *Nano Lett.* **2015**, *15*, 4071–4079.
[28] X. Sun, V. Duffort, B. L. Mehdi, N. D. Browning, L. F. Nazar, *Chem. Mater.* **2016**, *28*, 534–542.
[29] H. Y. Zhang, K. Ye, X. M. Huang, X. Wang, K. Cheng, X. Xiao, G. L. Wang, D. X. Cao, *J. Power Sources* **2017**, *338*,136–144.
[30] H. Y. Zhang, K. Ye, K. Zhu, R. B. Cang, X. Wang, G. L. Wang, D. X. Cao, *ACS Sustainable Chem. Eng.* **2017**, *5*, 6727–6735.
[31] H. Wang, L. F. Cui, Y. Yang, H. S. Casalongue, J. T. Robinson, Y. Liang, Y. Cui, H. Dai, *J. Am. Chem. Soc.* **2010**, *132*, 13978–13980.
[32] C. F. Liu, H. Q. Song, C. K. Zhang, Y. G. Liu, C. P. Zhang, X. H. Nan, G. Z. Cao, *Nano Res.* **2015**, *8*, 3372–3383.
[33] S. Kim, K. W. Nam, S. Lee, W. Cho, J. S. Kim, B. G. Kim, Y. Oshima, J. S. Kim, S. G. Doo, H. Chang, D. Aurbach,, J. W. Choi, *Angew. Chem.* **2015**, *54*, 15094–15099.
[34] S. Kim, S. Lee, K. W. Nam, J. Shin, S Y. Lim, W. Cho, K. Suzuki, Y. Oshima, M. Hirayama, R. Kanno, J. W. Choi, *Chem. Mater.* **2016**, *28*, 5488–5494.
[35] D. P. Dubal, D. S. Dhawale, R. R. Salunkhe, C. D. Lokhande, *J. Electroanal. Chem.* **2010**, *647*, 60–65.
[36] S. H. Guo, M. Zhang, G. N. Zhang, L. Zheng, L. P. Kang, Z. H. Liu, *Powder Technol.* **2012**, *228*, 371–376.
[37] Y. Dai, K. Wang, J. Y. Xie, *Appl. Phys. Lett.* **2007**, *90*, 104102.
[38] D. P. Dubal, D. S. Dhawale, R. R. Salunkhe, C. D. Lokhande, *J. Electrochem. Soc.* **2010**, *157*, A812–A817.
[39] J. Y. Qu, F. Gao, Q. Zhou, Z. Y. Wang, H. Hu, B. B. Li, W. B. Wan, X. Z. Wang, J. S. Qiu, *Nanoscale* **2013**, *5*, 2999–3005.
[40] Y. Q. Qiao, Q. J. Sun, H. Y. Cui, D. B. Wang, F. Y. Yang, X. H. Wang, *RSC Adv.* **2015**, *5*, 31942–31946.
[41] Y. Liu, Y. Qiao, X. D. Lou, X. H. Zhang, W. X. Zhang, Y. H. Huang, *ACS Appl. Mater. Interfaces.* **2016**, *8*, 14564–14571.
[42] K. M. Zhao, K. Z. Lyu, S. Q. Liu, Q. M. Gan, Z. He, Z. Zhou, *J. Mater. Sci.* **2017**, *52*, 446–457.
[43] Y. G. Wang, Y. Y. Xia, *Electrochem. Commun.* **2005**, *7*, 1138–1142.
[44] M. E. Orazem, B. Tribollet, Electrochemical Impedance Spectroscopy. *Electrochemical Impedance Spectroscopy* **2011**.

Manuscript received: June 14, 2018
Version of record online: August 9, 2018